Observational Constraints on the Identification of Shallow Lunar Magmatism: Insights from Floor-fractured Craters

L.M. Jozwiak[1], J.W. Head[1], G.A. Neumann[2], and L. Wilson[3]

[1]Dept. Earth, Environmental and Planetary Sciences, Brown University, Providence, RI 02912.
[2]Solar System Exploration Div., NASA Goddard Space Flight Center, Greenbelt, MD 20768.
[3]Lancaster Environment Centre, Lancaster University, Lancaster LA1 4YQ, UK.
(lauren_jozwiak@brown.edu)

Submitted to *Icarus*

July 13th, 2015

Abstract:

Floor-fractured craters are a class of lunar crater hypothesized to form in response to the emplacement of a shallow magmatic intrusion beneath the crater floor. The emplacement of a shallow magmatic body should result in a positive Bouguer anomaly relative to unaltered complex craters, a signal which is observed for the average Bouguer anomaly interior to the crater walls. We observe the Bouguer anomaly of floor-fractured craters on an individual basis using the unfiltered Bouguer gravity solution from GRAIL and also an degree 100-600 band-filtered Bouguer gravity solution. The low-magnitude of anomalies arising from shallow magmatic intrusions makes identification using unfiltered Bouguer gravity solutions inconclusive. The observed anomalies in the degree 100-600 Bouguer gravity solution are spatially heterogeneous, although there is spatial correlation between volcanic surface morphologies and positive Bouguer anomalies. We interpret these observations to mean that the spatial heterogeneity observed in the Bouguer signal is the result of variable degrees of magmatic degassing within the intrusions.

Keywords: Moon, Geophysics, Volcanism

I. Introduction:

Floor-fractured craters (FFCs) are a small subset of lunar craters with anomalously shallow, fractured floors [Schultz, 1976; Jozwiak et al., 2012]. FFCs range in diameter from ~10-200 km and frequently exhibit volcanic morphologies within the crater interior (vents, pyroclastic deposits, deposits of mare material). FFCs exhibit non-axisymmetric floor uplifts that are associated with a wide range of floor morphologies [Jozwiak et al., 2012]; smaller FFCs typically exhibit more domed floors, while larger FFCs generally exhibit flatter floors. These two floor morphologies represent end-member cases with all crater floor morphologies existing on a continuum between these end-members [Jozwiak et al., 2012]. FFCs are morphologically interpreted to be formed by the intrusion of a magmatic body beneath the crater floor [e.g. Schultz, 1976] formed by the propagation of a dike from depth that then stalls in the underdense brecciated region beneath the crater, and then spreads laterally to form a sill [Maccaferri et al., 2011; Jozwiak et al., 2015]. This hypothesis that is supported by morphologic and morphometric observations of the craters [Jozwiak et al., 2012; 2015a] made using LROC-WAC (Lunar Reconnaissance Orbiter Camera- Wide Angle Camera) [Robinson et al., 2010] images and LOLA (Lunar Orbiter Laser Altimeter) topographic data [Smith et al., 2010]. Key morphologic observations supporting the magmatic intrusion hypothesis include: volcanic morphologies within the craters (vents, pyroclastic deposits, deposits of mare material) and non-axisymmetric floor uplift [Jozwiak et al., 2012]. Key morphometric parameters supporting the magmatic intrusion hypothesis include the wide range of crater diameters the process affects (~10-200 km), and the preservation of short wavelength topography (i.e. crater rim crest heights) despite the significant relaxation of long wavelength topography (i.e. depth of the crater floor) [Jozwiak et al., 2012]. Recent implicit finite-volume modeling supports the hypothesis that FFCs are formed

by the intrusion of a volcanic body beneath a pinned elastic sheet (the overlying crust) [Thorey and Michaut, 2014].

It has long been proposed that the use of sufficiently high resolution gravity data could aid in understanding the mechanism by which floor-fractures craters form [Schultz, 1976], as well as in the identification of subsurface magmatic bodies that do not produce identifiable surface morphologies. Thus far, the identification of FFCs has always relied on surface morphologic evidence due to the low spatial resolution of available gravity data. The GRAIL (Gravity Recovery and Interior Laboratory) [Zuber et al., 2013] mission provides, for the first time, gravity field data of sufficient spatial resolution to investigate the gravity anomaly properties associated with FFCs.

Current analyses using the GRAIL data have focused on statistical assessments of Bouguer gravity anomalies associated with lunar impact craters. The Bouguer gravity anomaly is derived from the free-air gravity anomaly, but includes a correction for the gravitational signature of topography; thus, the resulting solution emphasizes density variations within the body. Soderblom et al. [2015] and Thorey et al. [2015] used the residual Bouguer anomaly for craters, which is computed by subtracting the average of the Bouguer anomaly from the floor of the crater from the average Bouguer anomaly from an annulus outside the crater, yielding the Bouguer anomaly relative to the surrounding region. Soderblom et al. [2015] examined the Bouguer gravity signatures of ~1200 complex highland craters and observed that the residual Bouguer anomalies of these craters are generally negative, but that the magnitude scales with crater diameter such that larger craters have more negative Bouguer anomalies. The data show that the range of Bouguer anomalies is ~ $\pm$ 30 mGal [Soderblom et al., 2015]. Thorey et al., [2015] performed a statistical analysis of Bouguer anomalies of FFCs compared with nearby complex craters. They determined that on average, FFCs have a more positive crater floor Bouguer anomaly than complex craters.

These statistical analyses support the hypothesis that there exist high density intrusions beneath floor-fractured craters, resulting in positive Bouguer anomalies. Thus far, the identification of floor-fractured craters and other shallow intrusive magmatic features (e.g. dikes) has been confined to places where they produce identifiable surface morphologies. The use of high-resolution gravity data could provide a new tool for the identification of shallow magmatic bodies on the Moon both in regions of suspected magmatic activity (e.g. beneath floor-fractured craters and graben), and also in regions where no surface expression was observed. Previous studies [Thorey et al., 2015] have shown that positive Bouguer anomalies can be associated with floor-fractured craters when the group is statistically analyzed in aggregate. We seek to address whether Bouguer anomalies can be used as analytic tools on individual targets. To this end, we begin by assessing several Bouguer anomaly gravity products for regions of known subsurface magmatic processes (ie. floor-fractured craters) to determine the utility of gravity data in identifying small, shallow magmatic bodies on the Moon. We then explore how the observed correlations between the Bouguer gravity data and the observed morphologies inform our

understanding of the floor-fractured crater intrusion formation process. Finally, we seek to address if Bouguer gravity data can be used in the identification of previously unrecognized shallow magmatic bodies on the Moon.

II. Predictions of FFC Gravity Signal:

The impact cratering process is generally assumed to produce a negative Bouguer anomaly within the crater, as a consequence of the intense fracturing and brecciation that occurs as a result of the impact-induced shock waves [e.g. Phillips et al., 1978]. This negative Bouguer anomaly has been observed in both terrestrial [e.g. Pilkington and Grieve, 1992] and young lunar craters [Dvorak and Phillips, 1977]. Recent studies using GRAIL data support the observation that the residual Bouguer anomaly in the crater generally exhibits increasingly negative values with increasing crater diameter [Soderblom, et al., 2015, submitted]. Results from the GRAIL mission suggest that the lunar crust has a density of 2560 kg/m^3 with an average porosity of 12% [Wieczorek et al., 2013]. Measurements of lunar basalt from Apollo samples, place the density of lunar basalts at 2900-3200 kg/m^3 depending on the TiO_2 content [Kiefer et al., 2012]. Thus, a crustal magmatic intrusion (like that proposed to be present below FFCs) composed of basaltic material is significantly denser than the average lunar crustal density, and is therefore predicted to produce a large positive Bouguer anomaly.

Before investigating the observed Bouguer anomaly of FFCs, we first model the predicted maximum anomaly using a simple Bouguer plate model for the archetypal FFCs Humboldt, Alphonsus, and Vitello. The model consists of a crater and surrounding subsurface environment with standard lunar crustal density, ρ_c=2560 kg/m^3, and a magmatic sill beneath the floor of the crater composed of lunar basalt, ρ_m=3000 kg/m^3. We assume that the degree of floor uplift represents the thickness of the intrusion, w_m [e.g., Jozwiak et al., 2012], and so we estimate w_m by subtracting the observed crater depth, d, from the theoretical crater depth, d_t. We find d by measuring the elevation difference between the average rim-crest height and floor elevation with LOLA data, and d_t is estimated from the fresh-crater depth-diameter relationships found by Pike [1980].

Using the simplifying assumptions of the Bouguer plate model, the maximum predicted BA is given by eq. 1,

$$BA = 2\pi(\rho_m - \rho_c)Gw_m, \quad (1)$$

where G is the gravitational constant. The results of this analysis for the crater Humboldt, Alphonsus, and Vitello are given in Table 1, and represent the maximum possible BA for each of these craters before subsequent band-filtering of the data. As expected, the BA is highly dependent on intrusion thickness, and is predicted to be in the range of tens to a few tens of mGal for w_m values between a few hundred meters and a few kilometers, consistent with the values generated by Thorey et al. [2015] from synthetic FFC geometries. The magnitude of the BA

predicted to be present at FFCs is thus well within the resolution of the GRAIL instrument (0.001 mGal) [Zuber et al., 2013].

Table 1:

Crater Name	Diameter [km]	d [m]	d_t [m]	w_m [m]	BA [mGal]
Humboldt	207	3200	5200	2000	36
Alphonsus	119	3500	4400	900	16
Vitello	44	2500	3200	700	13

III. Observations of FFC Bouguer Anomalies:

We conducted a survey of observed BA within FFCs using the Jozwiak et al. (2012) global catalog of FFCs (N = 170) and the GRGM900c Bouguer gravity solution [Lemoine et al., 2014] in the ArcGIS system. The resolution of the 900c model is ~6 km^2 [Lemoine et al., 2014], although due to the dominance of noise in the highest order terms, the data are limited to degree 600 which has a block size of ~ 9 km^2. The data were not filtered in any way beyond this, and the color stretch was applied to the entire range of lunar data, ~+600 mGal - ~-300 mGal.As a result of the model resolution, FFCs with diameter < 20 km were excluded from this analysis, as the floor region is oftentimes at or below the model solution resolution. This diameter restriction brings the number of observed craters to 122, 72% of the original catalog [Jozwiak et al., 2012]. The observations fell into three broad categories: 1) mascon dominated, 2) positive signal, 3) null signal; the frequency distribution of the data are shown in Figure 1. Many FFCs are located inside, or along the edges of large impact basins, consequently the Bouguer anomaly of the crater is completely overwhelmed by the gravity signal of the basin, these are termed “mascon dominated”, and account for 33% (40 craters) of the craters observed. The designation “positive signal” is used to identify craters that possess a positive central Bouguer anomaly, broadly correlated with the crater floor region, and account for 52% (64 craters) of the observed craters. The final category is “null signal” which denotes craters where the Bouguer anomaly is indistinguishable from the regional Bouguer anomaly. The threshold for distinction between “positive signal” and “null signal” is ± 5 mGal, which is a function of the global data color stretch, and represents distinct, discrete color values in the stretched dataset. The “null signal” designation is found predominately in smaller craters, D < 50 km, and accounts for 16% (18 craters) of the observed population. It is important to note that these categories are observational in nature and do not represent a statistical assessment of the magnitude of BA found in these FFCs; we direct readers seeking such a treatment to Thorey et al. [2015].

The results of this analysis suggest that there is some indication in the standardly released Bouguer gravity field for an association of positive Bouguer anomalies with floor-fractured craters, as would be predicted. Despite this, the assessment technique is non-ideal for conclusively identifying a link between Bouguer anomalies and shallow magmatic bodies on the

Moon. The two largest complications to analysis are 1) the inclusion of low-degree, high-magnitude terms in the gravity solution (e.g. mascons) which overpower the smaller signal of shallow magmatic intruions, and 2) the coarse resolution and averaging over features of interest smaller than several 10s km^2. Consequently, we turn to more advanced data filtering techniques to better isolate the gravity contributions of small, shallow magmatic bodies.

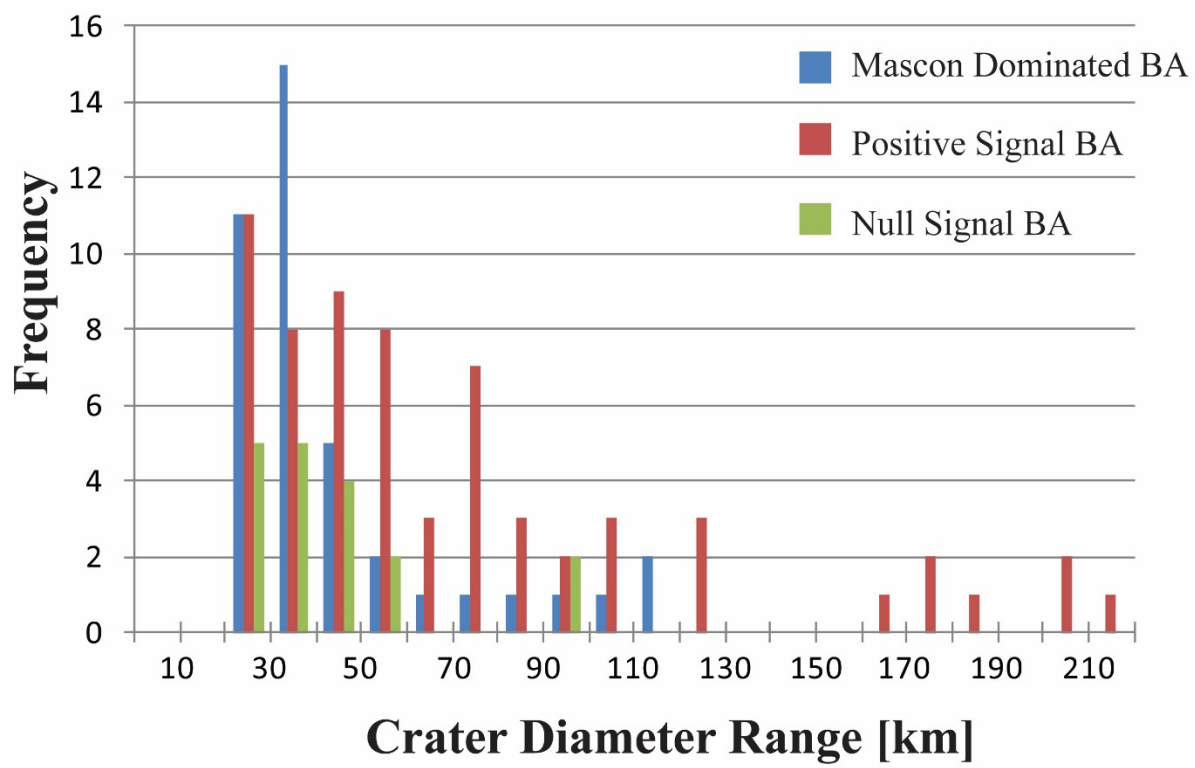

Figure 1: Qualitative, observational assessment of floor-fractured crater Bouguer anomaly for all floor-fractured craters with D> 20 km. Analysis yielded three categories of observed Bouguer anomaly: (1) mascon dominated, (2) positive signal, (3) null signal. (1) Mascon dominated signals were observed in craters located at the edges or interiors of basins, and are consequently characterized by the overwhelming basin Mascon gravity signature. (2) Positive signal denotes craters which possessed a positive Bouguer anomaly in the floor region, which was observed to be qualitatively higher than the regional Bouguer anomaly. (3) Null signal denotes craters with no inherent, identifiable Bouguer anomaly that is distinct from the regional Bouguer anomaly. Floor-fractured craters taken from Jozwiak et al., [2012]. Gravity data are the GRGM900c Bouguer gravity solution for the GRAIL data.

IV. Band-filtered Bouguer Anomaly:

The previous analysis with the GRGM900c Bouguer contains the spherical harmonic solutions for all degrees through degree 900. Gravity fields are dominated by low-degree contributions associated with long-wavelength perturbations to the gravity field and by perturbations to surfaces of density discontinuities (e.g. core-mantle boundary and the Moho) [Wahr, 1996]. This is also true of the Moon where below degree 80, most of the gravitational

signal is not attributable to topography, but rather to long-wavelength interior variations [Zuber et al., 2013]. Smaller-scale density variations, such as those associated with FFC intrusions, are only resolvable using the higher-order spherical harmonic solutions. Using the HigenX program, we band-filter the GRGM900c Bouguer spherical harmonic solution to degree 6-600 and also degree 100-600 solutions (Figure 2) to better emphasize the density anomalies within the crust. For both solutions, the upper limit of degree 600 was selected because it represents the highest degree solution with strong correlation and RMS power [Lemoine et al., 2014]. We selected a lower degree limit of degree 6 to remove spherical harmonic contributions from lunar oblateness and deviations in the center of mass, but retain most contributions to the gravity field from density disturbances in the crust and mantle. For the second model solution, a lower limit of degree 100 was selected to preferentially exclude gravity disturbances originating in the mantle, and thus focus on gravity disturbances in the crust. The degree 100-600 solution has a block size of ~9 km, and filtering the anomalies below degree 100 attenuates disturbances deeper than 34 km by a factor of 7.4 or more. Thus we assume that gravity anomalies in the degree 100-600 solution arise exclusively from density variations within the lunar crust, although mantle plug contributions could still be present in very large craters located in regions of thin crust (e.g., Oppenheimer). These density variations could be the result of compositional variation (e.g. basalt instead of anorthosite), or the result of variations in porosity. Because of the retention of high-magnitude low-degree mantle contributions, the degree 6-600 solution has difficulty showing low-magnitude, high-order features. This can be seen in a comparison of the dynamic range displayed in the degree 6-600 solution (Fig. 2a) as compared to the degree 100-600 solution (Fig. 2b). The constrained scale of the degree 100-600 solution allows us to focus on gravity disturbances with magnitude variations of < 5 mGal, which are muted to the point of invisibility in the degree 6-600 solution.

In Figure 2 we compare the solutions for the degree 6-600 solution (Fig. 2a) and degree 100-600 solution (Fig. 2b) for the crater Humboldt (27.2°S, 80.9°E), D = 207 km (Fig. 2c). The degree 6-600 solution has much higher magnitude gravity disturbances, including a broad 100 mGal gravity anomaly dominating a large portion of the crater floor region. This is consistent with the gravitational signature of an uplifted mantle plug, a signature which is observed in craters with D > 218$\pm$ 17 km [Soderblom et al., 2015]. In the degree 100-600 solution the broad positive anomaly we associated with the uplifted mantle plug is no longer observed. Instead, numerous lower magnitude gravity disturbances emerge and appear heterogeneously distributed throughout the crust in the field of view. The low-magnitude nature of these anomalies is problematic when observed in the degree 6-600 solution because the magnitudes of the low-degree anomalies are significantly larger and overwhelm the intrusive volcanic signal. In section II we calculated theoretical maximum magnitudes for the BAs associated with FFC intrusions, and all of these magnitudes are an order of magnitude smaller than the typical BA displayed by low-degree mantle features like mascons. Thus, although the degree 6-600 band-filtered solution eliminates some of the noise from the GRGM900c Bouguer model, it does not prove useful in the identification of small-scale magmatic anomalies. For this reason, we now focus on the

results of the degree 100-600 band-filtered solution, which greatly attenuates the low-degree, high-magnitude contributions to the gravity field.

Within the crater Humboldt, there emerge two regions of positive gravity anomalies with magnitudes of ~15 mGal . These regions are broadly correlated with the surface locations of 3 of the observed mare deposits on the floor of Humboldt crater. The mare deposits are indicated by black arrows in both the degree 100-600 solution (Fig. 2b) and the LROC-WAC image of Humboldt crater (Fig. 2c). None of these surficial volcanic deposits would be expected to produce a gravity anomaly of the observed magnitude because of their limited thickness (< few hundred meters). We suggest this correlation of positive gravity anomaly regions with regions hosting volcanic morphologies could be indicative of the subcrater magmatic body which produced the surface volcanic deposits. We note, however, that numerous Bouguer anomalies of comparable magnitude are present (outside of the crater) which are not associated with surface volcanic features. The provenance of these exterior anomalies cannot be explained by associations with any unique surface morphologies We instead focus our attention on Bouguer anomalies arising in the crater floor region, because for these anomalies we have a hypothesis for the main contribution to the Bouguer anomalies—the density changes associated with the sub-crater shallow magmatic intrusion.

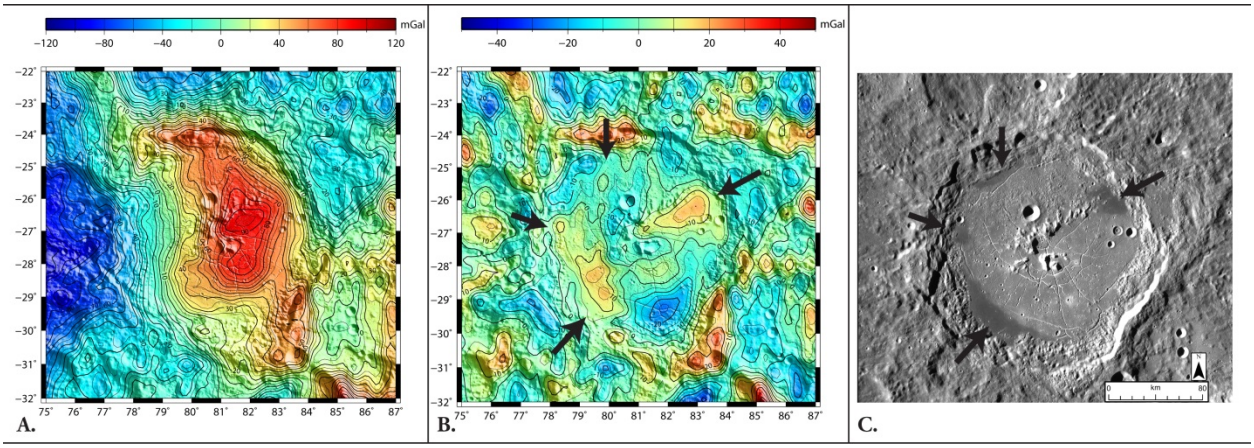

Figure 2: A comparison of band-filtered Bouguer gravity solutions for the crater Humboldt (D = 207 km) (27.2°S, 80.9°E). **A**) The band-filtered Bouguer solution from degrees 6-600 reveals a broad, high positive anomaly slightly offset from the center of the crater. Due to the large diameter of Humboldt, some portion of this anomaly is attributable to mantle uplift processes [Soderblom et al., 2015]. **B**) The band-filtered Bouguer solution from degrees 100-600 represents almost exclusively crustal density variations. The surface volcanic deposits on the floor of Humboldt have been marked with black arrows. The large anomaly observed in **A**. has been removed by the filtering; instead, three smaller provinces of positive Bouguer anomaly emerge. These three regions are spatially correlated with surface volcanic morphologies in Humboldt.**C)** LROC-WAC image of Humboldt crater with the surface volcanic deposits indicated by black arrows, as in **B**. The band-filtered Bouguer solutions were generated from the GRGM900c Bouguer solution to GRAIL data.

We extend our band-filtering analysis to all FFCs with D > ~100 km, including the craters Oppenheimer, Humboldt, Janssen, Gauss, Petavius, Compton, Cleomedes, Nernst,

Alphonsus, Gassendi, Repsold, Posidonius, and Schlüter. We focused our analysis on larger craters (D > 100 km) so as to maximize the spatial block resolution over the crater floor region. In the regions outside of the craters, we observed a persistently heterogeneous signal in the degree 100-600 filtered Bouguer solution. Inside of the craters, we also observed heterogeneities in the gravity disturbances. However, much like our observations at Humboldt, the regions of positive gravity disturbances on the crater floor appear to be spatially correlated with either surficial volcanic morphologies (i.e. mare deposits and pyroclastic deposits) or heavily fractured floor regions. The crater Alphonsus demonstrates some degree of spatial correlation between regions with positive Bouguer anomalies on the crater floor and surficial volcanic morphologies (Fig. 3). Alphonsus hosts several well-defined fractures and pyroclastic deposits in the eastern half of the crater floor, with a large portion of the pyroclastic deposits located in the northeast portion of the crater floor. This region is spatially correlated with a large positive Bouguer anomaly located in the eastern half of the crater, and concentrated in the northeastern part of the crater floor (arrows in Fig. 3). Despite the correlations in the northeast portion of the crater floor, the pyroclastic deposit located in the southeastern portion of the crater floor correlates to a region of approximately 0 mGal BA, and the pyroclastic deposits in the western portion of the crater floor are adjacent to a regional BA low.

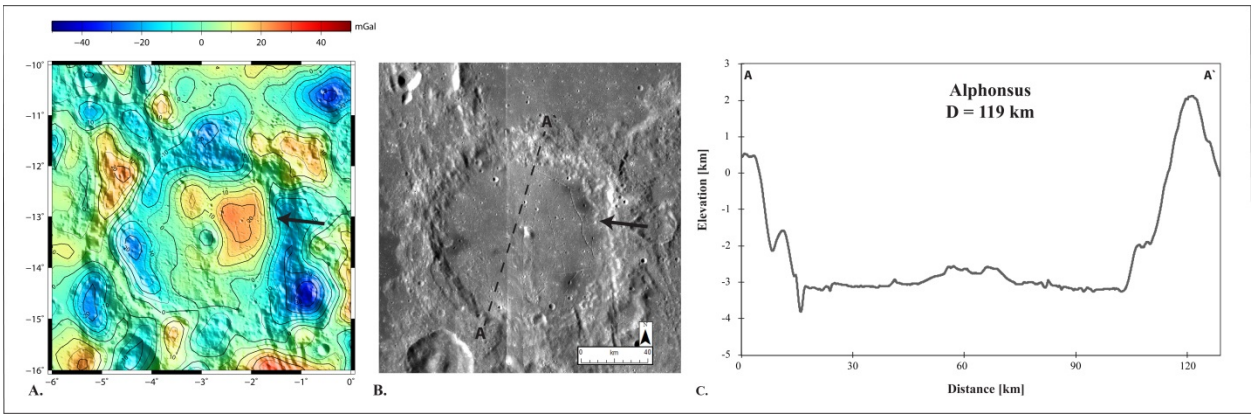

Figure 3: The crater Alphonsus (D = 119 km) (13.4°S, 2.8°W) **A**) degree 100-600 band-filtered Bouguer anomaly reveals a broad positive Bouguer anomaly within the crater floor, and a concentrated region of higher Bouguer anomaly in the northeast quadrant of the crater, indicated by the black arrow. This anomaly corresponds spatially with a region of numerous fractures and pyroclastic deposits on the crater floor, indicated by the arrow in **B**. Conversely, neither the pyroclastic deposit in the southeast portion of the crater floor, nor the deposits in the western portion of the crater floor correlate with strong positive BA. **C**) A topographic profile across Alphonsus shows a flat floor, indicating uniform uplift across the crater floor. **A**) Generated from GRGM900c Bouguer solution to GRAIL data. **B**) LROC-WAC (Lunar Reconnaissance Orbiter Camera- Wide Angle Camera) image. **C**) LOLA (Lunar Orbiter Laser Altimeter) data.

We continued our analysis of the degree 100-600 band-filtered gravity solution to several of the floor-fractured craters with D > 100 km (Fig. 4), we examined both the degree of heterogeneity, and also correlations between gravity anomalies and surface volcanic morphologies (mare deposits and pyroclastic deposits [Gaddis et al., 2003]). The craters

Gassendi (Fig. 4g, h) and Cleomedes (Fig. 4c, dm), which are located at the edges of Humorum and Crisium basin, respectively, show large magnitude, linear positive anomalies. These are interpreted as large, older circumbasin dikes, first identified in GRAIL data by Andrews-Hanna et al. [2013], and are not related to the shallow intrusions we are addressing here. The data show a general correlation of positive Bouguer anomalies beneath regions hosting volcanic surface morphologies. Examples of this can be seen in the eastern half of Alphonsus (Fig. 4a, b), Compton (Fig. 4e, f), Gauss (Fig. i, j), Humboldt (Fig. k, l), and Petavius (Fig. o, p). However notable deviations occur in the western half of Alphonsus, and in Cleomedes crater. Neither Gassendi crater, nor Janssen crater have surface volcanic morphologies, although both do have a broadly positive interior Bouguer anomaly.

Given the extreme heterogeneity we observed in the FFC Bouguer anomaly, we examined whether or not the statistically observable difference between FFC and complex crater Bouguer anomalies [Thorey et al., 2015] was observable in the individual data, either in terms of overall magnitude or in terms of degree of heterogeneity. We examined a randomly selected set of complex craters with D > 100 km, and stratigraphic ages spanning from the pre-Nectarian to Upper Imbrian, which represent the range in stratigraphic ages for most FFCs [Jozwiak et al., 2015a] (Fig. 5). We applied the same band-filtering technique that was applied to the FFCs. We found that the regions outside of the craters maintained similar levels of heterogeneity observed in regions outside of FFCs. Inside the crater, the gravity anomalies display heterogeneities similar to those observed on the floors of FFCs. Unlike FFCs, however, there is no observed spatial correlation of gravity anomalies with surface morphologies in the complex craters. We note that because the complex craters lack many of the distinctive floor morphologies of FFCs, the lack of correlation between morphologic features and gravity anomalies is unsurprising. When viewed next to FFCs (Fig. 4), it is difficult to identify complex craters (Fig. 5) using only the observed gravity anomalies . Although FFCs have a more positive Bouguer anomaly than complex craters on average [Thorey et al., 2015], the heterogeneous nature of the lunar crust (as seen through gravity data) necessitates that geologic data (such as LOLA and LROC) be used in conjunction with the gravity data to verify the presence of suspected magmatic intrusions.

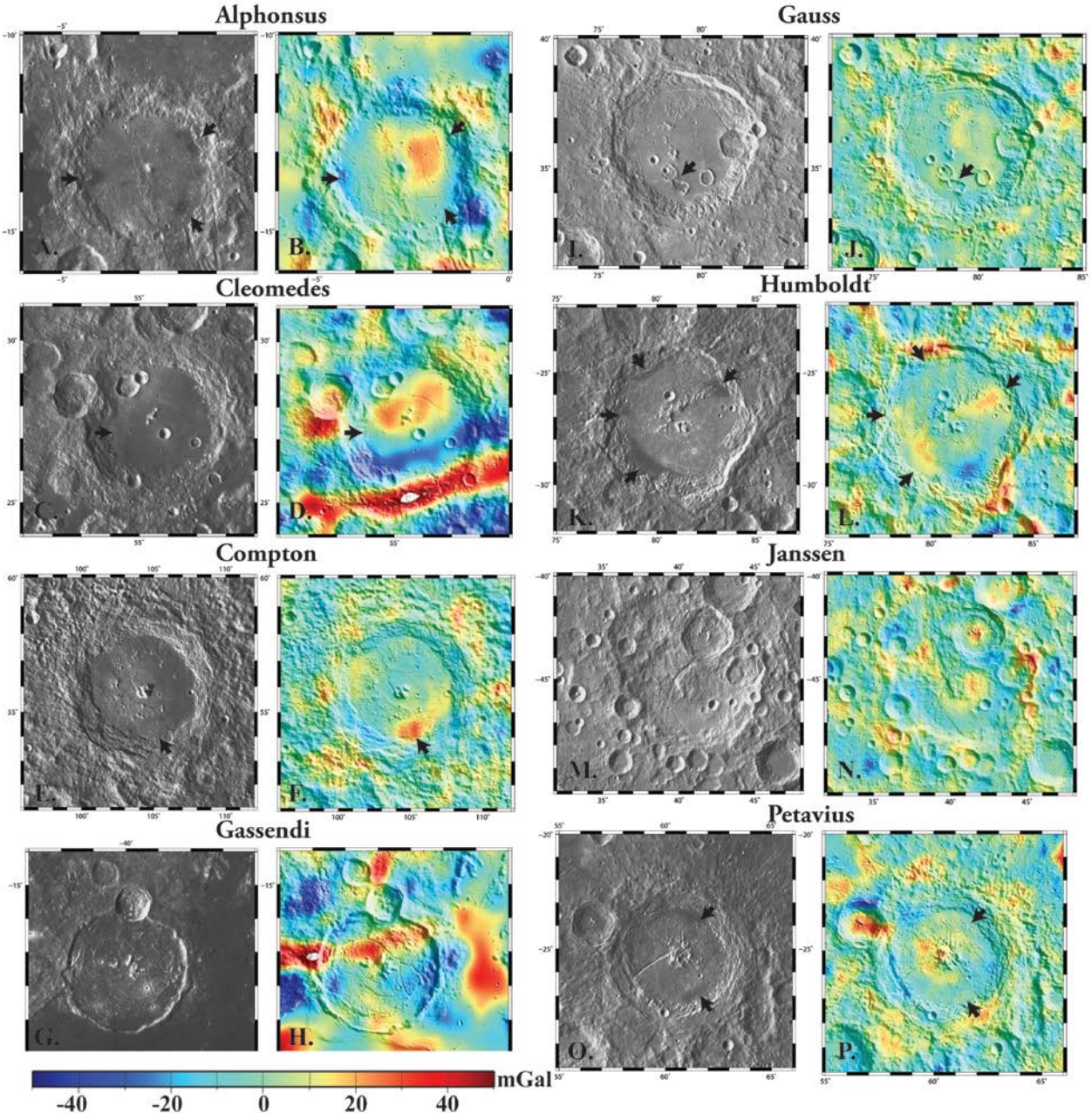

Figure 4: Images of eight floor-fractured craters compared to the degree 100-600 band-filtered Bouguer anomalies for each crater.. Surface volcanic morphologies including mare deposits and pyroclastic deposits (as identified in Gaddis et al. [2003]) are noted with black arrows in both the visual image and the band-filtered gravity solution. All craters display a heterogeneous Bouguer anomaly. Many of the regions beneath and adjacent to surface volcanic morphologies are correlated with regions of positive Bouguer anomaly, although there are notable exceptions in the western part of Alphonsus crater and in Cleomedes crater. . Alphonsus crater image (a), gravity (b); Cleomedes crater image (c), gravity (d); Compton crater image (e), gravity (f); Gassendi crater image (g), gravity (h); Gauss crater image (i), gravity (j); Humboldt crater image (k), gravity (l); Janssen crater image (m), gravity (n); and Petavius crater image (o), gravity (p). All visual images are LROC-WAC images in sinusoidal projection, centered on the crater center longitude.

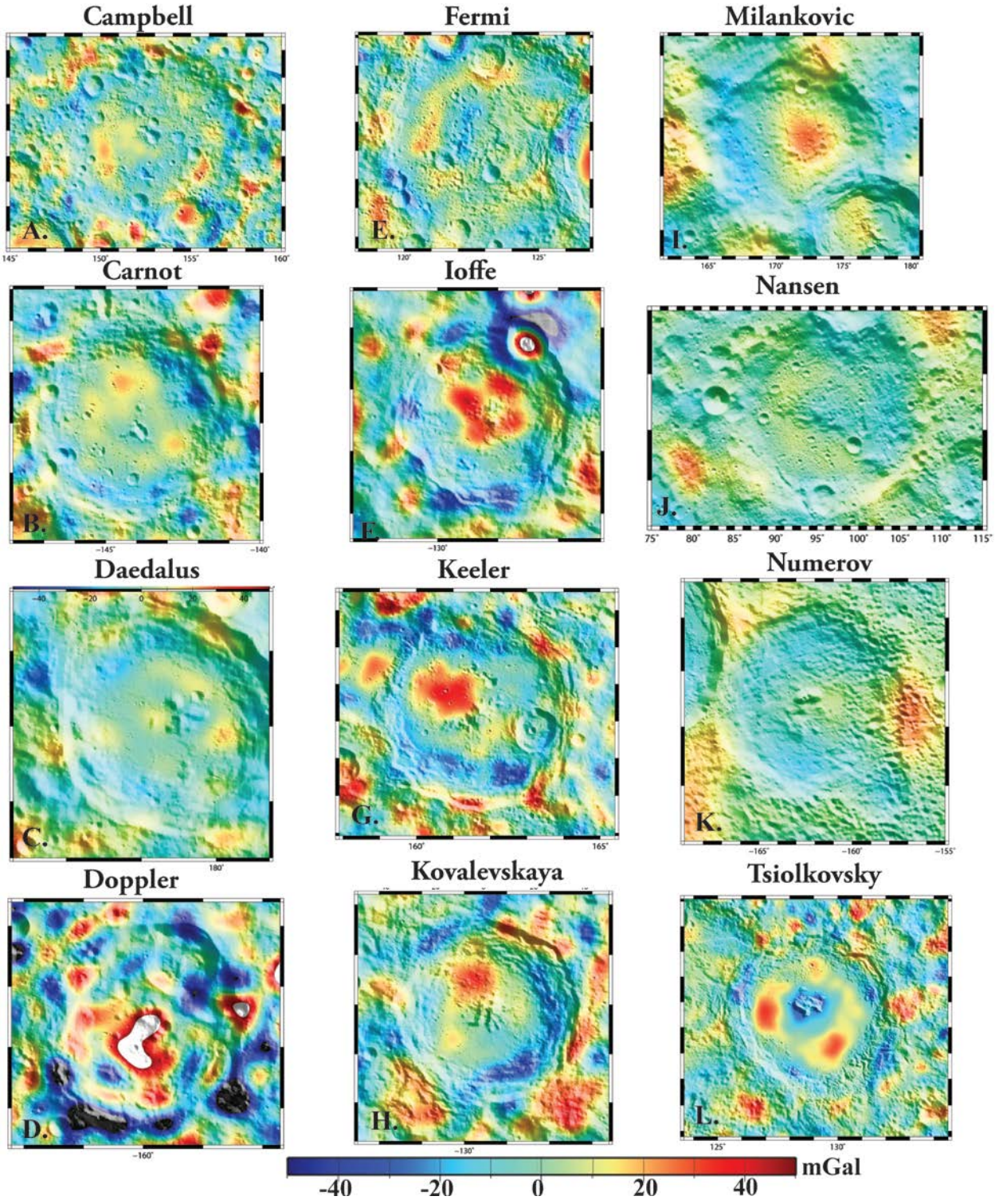

Figure 5. GRAIL Bouguer gravity data band-filtered to degree 100-600 for 12 complex lunar craters. All craters data are shown at the same scale, which is consistent with the scale used in Fig. 4. The complex craters exhibit a variety of heterogeneities in the band-filtered degree 100-600 solution, however, these heterogeneities are not correlated with any distinct surface morphologies. The exception is the crater Tsiolkovsky (l), which has significant mare flooding over the entirety of the crater floor, and still displays some degree of heterogeneity, likely associated with

varying mare deposit thickness. A) Campbell, B) Carnot, C) Daedalus, D) Doppler, E) Fermi, F) Ioffe, G) Keeler, H) Kovalevskaya, I) Milankovic, J) Nansen, K) Numerov, L) Tsiolkovsky.

V. Discussion:

Both the morphologic analyses of FFCs [e.g. Jozwiak et al., 2015a] as well as statistical assessments of FFC Bouguer anomalies [Thorey et al., 2015] support the hypothesis that FFCs are formed by the intrusion of a magmatic body beneath the crater. The spatially heterogeneous Bouguer anomalies observed within individual craters, however, vary significantly from the spatial BA pattern predicted from both simple plate models (eq. 1) and synthetic sill models [Thorey et al., 2015], which both assume an axisymmetric sill intrusion geometry. The deviation between the spatial pattern (and magnitude) of observed Bouguer anomaly from the predicted Bouguer anomaly suggests that the model neglects some facet of the intrusion process. Possible hypotheses to explain the observed Bouguer anomaly heterogeneity include (1) spatial variations in intrusion geometry (i.e., an intrusion that does not extend beneath the entire crater floor, but is instead discretely located); and (2) spatial variations in intrusion density. In the case of variations in intrusion geometry, the intrusion does not fill the entire crater floor, but is instead located directly beneath the regions which have a positive Bouguer anomaly. We find this hypothesis unlikely because morphologic and morphometric analyses of FFCs [Jozwiak et al., 2012] indicate that the intrusions extend to the edges of the crater floor, and deform the entire overlying floor region, uplifting it either into a domed morphology or lifting the entire floor region in a competent piston-like fashion (Fig. 3c).

In the second scenario, the observed heterogeneity in the Bouguer anomaly may be the result of density variations within the intrusion. The evolution of magmatic intrusions involves a number of processes including solidification/contraction, crystal settling, bubble formation, and degassing [e.g. Marsh, 1989]. These last two processes, in particular, have a large effect on overall intrusion density, as there can be a large difference in the densities of degassed and non-degassed basalt. The listed basalt densities of 2900-3200 kg/m^3 [Kiefer et al., 2012] represent completely degassed basaltic samples. New research on returned Apollo glass samples, however, has revealed a significant volatile component in pre-eruption lunar magmas [Saal et al., 2008]. An additional and more volumetrically significant source of volatiles in shallow lunar magmatic intrusions is CO. CO is produced in the shallow lunar subsurface via pressure-dependent reduction reactions between metal oxides (i.e. Cr_2O_3, FeO, and Ti_2O_3) and $C_{graphite}$ in the melt [Sato, 1979; Fogel and Rutherford, 1995]. During the dike propagation process, bubbles will collect in the low-pressure dike-tip environment, forming a magmatic foam [Head et al., 2002; Wilson and Head, 2003].

The presence of pyroclastic deposits in many FFCs [e.g. Gaddis et al., 2003] provides ready evidence for the degassing of FFC magmatic intrusions. Using the observed range of pyroclastic material from the source vent, we can calculate the average gas volume fraction of the foam. The crater Alphonsus hosts several pyroclastic deposits with an average radius of 3-4

km [Head and Wilson, 1979]. The average velocity of pyroclastics, *v*, can be calculated from the following equation [Head et al., 2002; Wilson and Head, 2016],

$$R = \frac{v^2}{g} \quad (1)$$

where *R* is the deposit radius in meters and *g* is 1.62 m/s^2, the lunar acceleration due to gravity. The velocity can then be used to calculate the magmatic volatile gas fraction, *n*, from equation 2,

$$n = \left[\frac{v^2 m(\gamma-1)}{2QT\gamma}\right]^{\frac{1}{2}} \quad (2)$$

which represents a compromise between adiabatic gas expansion and gas expansion in a Knudsen regime [Wilson et al., 2014; Wilson and Head, 2016]. In this application, *m*, the gas molecular weight, is 28 kg mol^{-1}, *Q*, is the universal gas constant, 8314 J K^{-1} kmol^{-1}, *T* is the magmatic temperature, 1500 K, and γ is the ratio of gas specific heats, 1.28 (a weighted average of the two most common volatiles species, CO and H_2O) [Wilson et al., 2014; Jozwiak et al., 2015b].

From this analysis, the average range of pyroclasts in Alphonsus suggests a gas fraction of 0.0345, a volume fraction of 72.8% [Jozwiak et al., 2015b], which is well within the range of critical gas volume fraction for bubble collapse observed experimentally by Jaupart and Vergniolle [1989]. The density of CO at magmatic temperatures and pressures is 40 kg/m^3 [Wilson et al., 2014], which combined with the basalt, results in a foam density of 845 kg/m^3. The overall intrusion density can thus be deduced from a simple linear mixing of magmatic foam volume and degassed magma volume. For example, assuming a degassed basalt density of 3000 kg/m^3, and intrusion with 5% foam would have an overall density of ~2900 kg/m^3, whereas an intrusion with 25% foam would have an overall intrusion density of ~2450 kg/m^3. Thus, the amount of magmatic foam within an intrusion can have a significant effect on the intrusion density and by extension, the observed Bouguer anomaly. This hypothesis is also supported by the spatial correlation of surface volcanic morphologies with positive Bouguer anomalies. The volcanic features provide direct evidence of degassing within the underlying intrusion, suggesting that the removal of the magmatic foam component (through degassing) results in a higher positive Bouguer anomaly. In regions where there are no surficial volcanic morphologies, there is no direct evidence for the removal or collapse of the magmatic foam component, which results in a lower density for the region in question, and a correspondingly lower magnitude Bouguer anomaly. Although the wide range of observed Bouguer anomalies in complex craters [Soderblom et al., 2015] prevents the back-calculation of the foam volume in any given intrusion, work is ongoing to determine the amount of magmatic foam generated during the magma ascent process [Wilson and Head, 2016]. Future work may then provide constraints on the volume of solidified foam remaining within the intrusion [Jozwiak et al., *in prep*].

VI. Conclusions:

Morphologic studies using LROC and LOLA data provide evidence that the class of lunar craters called floor-fractured craters is formed by the intrusion of a magmatic body beneath the crater floor [Jozwiak et al., 2012, 2015a]. This interpretation is broadly supported by recent modeling work [Thorey and Michaut, 2014] and statistical analysis of floor-fractured crater Bouguer anomalies, which are on average more positive than those measured within complex craters [Thorey et al., 2015], consistent with the intrusion of a high density magmatic body beneath the crater floor. Although high resolution gravity data from GRAIL was initially postulated to provide a powerful analytic tool for these shallow magmatic intrusions, our analysis shows that great care must be exercised when applying gravity data to the investigation of shallow lunar magmatism. Our simple Bouguer plate modeling shows that, while the subcrater magmatic intrusions are capable of producing Bouguer anomalies resolvable by the GRAIL instrument, the overall magnitude of these anomalies is significantly smaller than most of the low-degree, high-magnitude contributions to the gravity field. This is borne out by assessments using both the raw GRGM900c Bouguer gravity model and a band-filtered degree 6-600 solution. In both of these analyses, although there was some correlation of floor-fractured craters with positive Bouguer anomalies, the correlation was not strong enough to serve as a predictive tool. To remove the effects of low-degree contributions to the gravity field, we also explored a band-filtered degree 100-600 gravity solution. When observed using the degree 100-600 solution craters displayed a spatially heterogeneous Bouguer anomaly signal, which is inconsistent with the predicted Bouguer anomaly based on the inferred intrusion morphology [Jozwiak et al., 2012] and on synthetic gravity modeling [Thorey et al., 2015]. The heterogeneities within the crust can be attributed to some combination of compositional variations and porosity variations. We observe, in the degree 100-600 solution, that within floor-fractured craters, regions of relatively high magnitude, positive Bouguer anomalies are spatially correlated with surface volcanic morphologies. We postulate that the observed heterogeneities in the Bouguer anomaly of floor-fractured craters arise as a natural consequence of the intrusion evolution and degassing process, wherein heterogeneous degassing of a magmatic foam results in localized areas of high Bouguer anomalies. Future work seeks to constrain the volume of foam produced during the dike propagation process, and its applicability to the evolution of shallow magmatic intrusions.

Acknowledgments:

We gratefully acknowledge the support of NASA Harriet G. Jenkins Fellowship (Grant NNX13AR86H) to L.M. Jozwiak. We also gratefully acknowledge financial support from the NASA Lunar Reconnaissance Orbiter (LRO) Mission, Lunar Orbiter Laser Altimeter (LOLA) Experiment Team (Grants NNX11AK29G and NNX13AO77G), the NASA Gravity Recovery and Interior Laboratory (GRAIL) Mission Guest Scientist Program (Grant NNX12AL07G) and the NASA Solar System Exploration Research Virtual Institute (SSERVI) grant for Evolution and Environment of Exploration Destinations under cooperative agreement number NNA14AB01A at Brown University. Additionally, we acknowledge Jay Dickson for his invaluable assistance in data processing.

454 References:

455 Andrews-Hanna, J.C., et al., 2013. Ancient igneous intrusions and early expansion of the Moon
456 revealed by GRAIL gravity gradiometry. Science 339, 675-678.

457 Dvorak, J., Phillips, R.J., 1977. The nature of the gravity anomalies associated with large young
458 lunar craters. GRL 4, 380-382.

459 Fogel, R.A., Rutherford, M.J., 1995. Magmatic volatiles in primitive lunar glasses: I. FTIR and
460 EPMA analyses of Apollo 15 green and yellow glasses and revision of the volatile-
461 assisted fire-fountain theory. Geochim. et Cosmochim. Acta 59. 201-125.

462 Gaddis, L. R., Staid, M. I., Tyburczy, J. A., Hawke, B. R., Petro, N. E., 2003, Compositional
463 analyses of lunar pyroclastic deposits. Icarus 161, 262-280.

464 Head, J.W., Wilson, L., Weitz, C.M., 2002. Dark ring in southwestern Orientale Basin: Origin as
465 a single pyroclastic eruption. J. Geophys. Res. 107. E1. 5001.

466 Jaupart, C., Vergniolle, S., 1989. The generation and collapse of a foam layer at the roof of a
467 basaltic magma chamber. J. Fluid Mech. 203. 347– 380.

468 Jozwiak, L.M., Head, J.W., Zuber, M.T., Smith, D.E., Neumann, G.A., 2012. Lunar floor-
469 fractured craters: classification, distribution, origin and implications for magmatism and
470 shallow crustal structure. J. Geophys. Res. 117. E11.

471 Jozwiak, L.M., Head, J.W., Wilson, L., 2015a. Lunar floor-fractured craters as magmatic
472 intrusions: geometry, modes of emplacement, associated tectonic and volcanic features,
473 and implications for gravity anomalies. Icarus 248. 424-447.

474 Jozwiak, L.M., Head, J.W., Neumann, G.A., Wilson, L., 2015b, The effect of evolving gas
475 distribution on shallow lunar magmatic intrusion density: implications for gravity
476 anomalies. LPSC XLVI, Abstract #1580.

477 Jozwiak, L.M., Head, J.W., Wilson, L., 2015. The evolution of shallow magmatic intrusions
478 beneath lunar floor-fractured craters and implications for intrusion eruption history.
479 Icarus, *In preparation.*

480 Kiefer, W.S., Macke, R. J., Britt, D. T., Irving, A. J., Consolmagno, G. J., 2012. The density and
481 porosity of lunar rocks. Geophys. Res. Lett., 39. L07201.

Lemoine, F.G., et al., 2014. GRGM900C: a degree 900 lunar gravity model from GRAIL primary and extended mission data. GRL 41. 3382-3389.

Maccaferri, F., Bonafede, M., Rivalta, E., 2011, A quantitative study of the mechanisms governing dike propagation, dike arrest, and sill formation. J. Vol. Geotherm. Res. 208, 39-50.

Marsh, B.D., 1989. Magma Chambers. Annu. Rev. Earth Planet. Sci. 17. 439-474.

Phillips, R.J., Abbott, E.A., Sjogren, W.L., Zisk, S.H., 1978. Simulation gravity modeling to spacecraft tracking data. Analysis and application to lunar crater anomalies. JGR 83, B11, 5455-5464.

Pike, R.J., 1980. Geometric interpretation of lunar craters. U.S. Geol. Surv. Prof. Paper, 1046-C. C1- C77.

Pilkington, M., Grieve, R.A.F., 1992. The geophysical signature of terrestrial impact craters. Rev. Geophys. 30. 2. 161-181.

Robinson, M.S., 2010. Lunar Reconnaissance Orbiter Camera (LROC) Instrument Overview. Space Sci. Rev. 150, 81-124.

Sato, M., 1979. The driving mechanism of lunar pyroclastic eruptions inferred from the oxygen fugacity behavior of Apollo 17 orange glass. Proc. Lunar Planet. Sci. X, 311-325.

Schultz, P.H., 1976. Floor-fractured lunar craters, The Moon 15, 241-273.

Smith, D.E, 2010. The Lunar Orbiter Laser Altimeter investigation on the Lunar Reconnaissance Orbiter mission. Space Sci. Rev. 150, 209-241.

Soderblom, J.M., et al., 2015. Production and saturation of porosity in the lunar highlands from impact cratering. Nature Geoscience *Submitted*.

Thorey, C., Michaut, C., 2014. A model for the dynamics of crater-centered intrusion: application to Lunar floor-fractured craters. J. Geophys. Res. Planets. DOI: 10.1002/2013JE004467.

Thorey, C., Michaut, C., Wieczorek, W., 2015. Gravitational signatures of lunar floor-fractured craters. EPSL 424, 269-279.

Wahr, J., 1996. Geodesy and Gravity. Samizdat Press, Golden, CO.

Wieczorek, M.A., et al., 2013. The crust of the Moon as seen by GRAIL, Science 339, 671-675.

Wilson, L., Head, J.W.,2003. Deep generation of magmatic gas on the Moon and implications for pyroclastic eruptions. GRL 30, 1605.

Wilson, L., Head, J.W., Tye, A.R., 2014. Lunar regional pyroclastic deposits: evidence for eruption from dikes emplaced in the near-surface crust. LPSC XLV, Abstract #1223.

Wilson, L., Head, J.W., 2016. Generation, ascent and eruption of magma on the Moon: new insights into source depths, magma supply, intrusions, and effusive/explosive eruptions (Part 1: Theory). Icarus *In Press.*

Zuber, M.T., et al., 2013. Gravity Recovery and Interior Laboratory (GRAIL): mapping the lunar interior from crust to core. Space Sci. Rev. 178. 3-24.

Zuber, M.T., et al., 2013. Gravity field of the Moon from the Gravity Recovery and Interior Laboratory (GRAIL) Mission. Science 339, 668-671.